component will be only 50 Ry, for a total of 400 Ry (*25*). The subsolar intensity is approximately 1500 Ry, so that the remaining 1 kRy must be collisionally excited.

The H Lyman α emission intensity from the nightside of Uranus, in the nonauroral regions, is at least 170 Ry and may be variable. Resonance scattering of emissions from the interstellar medium from a column abundance of 5×10^{16} cm^{-2} at 750 K will contribute only 100 Ry. A column abundance of 4×10^{17} cm^{-2} is required to produce 170 Ry. Such a large column abundance is unlikely, so that other excitation mechanisms such as radiative transfer from the dayside via the H corona and collisional excitation must be considered.

We have made a marginal detection of He 584 Å in resonance scattering of the solar line by helium in the Uranian atmosphere. With the UVS field filled by the sunlit hemisphere, a 10^5-second integration yields an intensity of 0.11 ± 0.08 Ry. This intensity corresponds to an eddy diffusion coefficient less than 3×10^7 cm^2 sec^{-1}.

Ultraviolet albedo of the atmosphere of Uranus. Longward of 1500 Å, the spectrum of Uranus is dominated by sunlight reflected by the atmosphere. Sunlight is scattered by both the gases and particulates, and its spectrum is modified by hydrocarbon absorption. Model calculations for Jupiter (*8*) fit spectra from both Jupiter and Saturn equally well at the resolution of the UVS (*10, 14*). Uranus has a higher far ultraviolet albedo than either Jupiter or Saturn and hence may be expected to show the effects of C_2H_2 in the gaseous as well as the condensed phase. We estimate that sunlight at 1490 Å penetrates to 0.5 to 1.0 mbar, through a vertical column abundance of C_2H_2 in the range 1×10^{17} to 3×10^{17} cm^{-2} with a mixing ratio of about 2×10^{-7} (*17*). In the model, sunlight at 1600 Å penetrates to 56 mbar through a column abundance of C_2H_2 less than 5×10^{17} cm^{-2}. Initial analysis indicates that condensation of C_2H_2 in the lower stratosphere may be required (*5*) to explain the spectrum, as was the case with the IUE spectra (*4*).

Other features. The spectrum of Uranus in Fig. 3 contains discrete emission features that correspond approximately to neutral carbon transitions at 1657, 1560, 1329, and 1280 Å. The estimated brightness of the feature at 1657 Å is about 50 Ry. A 1280-Å emission feature is also produced by Raman scattering of the solar H Lyman α line in H_2.

REFERENCES AND NOTES

1. In comparing the occultation light curves at various latitudes, we used an equilibrium figure for the planet that was calculated assuming GM = 5,793,920 km^3 sec^{-2} (G, universal gravitational constant; M mass), a rotation period of 17.3 hours, and $J_2 = 3.346 \times 10^{-6}$ and $J_4 = 3.21 \times 10^{-5}$.
2. In the analysis of these observations, we followed the procedure established by G. R. Smith *et al.*, *J. Geophys. Res.* **88**, 8667 (1983).
3. B. D. Savage *et al.*, *Astrophys. J.* **216**, 291 (1977).
4. Th. Encrenaz *et al.*, *Astron. Astrophys.*, in press.
5. S. K. Atreya, in *Uranus and Neptune*, J. T. Bergstralh, Ed. (*NASA Conf. Publ.* **2330**, 1984), p. 55.
6. R. G. French *et al.*, *Icarus* **53**, 399 (1983).
7. A. L. Broadfoot *et al.*, *Science* **204**, 979 (1979).
8. B. R. Sandel *et al.*, *ibid.* **215**, 548 (1982).
9. G. R. Smith *et al.*, *J. Geophys. Res.* **88**, 8667 (1983).
10. D. E. Shemansky, *ibid.* **90**, 2673 (1985).
11. ——— and G. R. Smith, *Geophys. Res. Lett.* **13**, 2 (1986).
12. D. M. Hunten *et al.*, in *Saturn*, T. Gehrels and M. S. Matthews, Eds. (Univ. of Arizona Press, Tucson, 1984), p. 671.
13. Several aspects of the H_2 models depend on recent unpublished work by A. J. Ajello, D. E. Shemansky, Y. L. Yung, A. Dalgarno, S. Guberman, T. L. Kwok, and A. Posen (1986).
14. D. E. Shemansky and J. M. Ajello, *J. Geophys. Res.* **88**, 459 (1983).
15. The energy distribution of the exciting electrons should be nearly Maxwellian because electron-electron relaxation is rapid; this distribution was used for our calculated spectra. The threshold for excitation of the H_2 emissions is about 10 eV, so that the excitation in this model is caused by electrons in the high-energy tail of the Maxwellian distribution. These electrons also dissociate H_2 and heat the atmosphere. The ratio of the H production rate to the ionization rate, which depends on the electron temperature, is ten times higher at Uranus than at Saturn. The total rates of production of escaping H are comparable at Uranus and Saturn.
16. The H_2 column abundance is inferred from self-absorption in the spectrum.
17. D. E. Shemansky, D. F. Strobel, Y. L. Yung, in preparation.
18. J. H. Waite *et al.*, *J. Geophys. Res.* **88**, 6143 (1983).
19. R. V. Yelle, B. R. Sandel, D. E. Shemansky, S. Kumar, *J. Geophys. Res.*, in press.
20. K. M. Hagenbuch and R. E. Hartle, *Phys. Fluids* **12**, 1551 (1969).
21. B. A. Smith *et al.*, *Science* **233**, 43 (1986).
22. R. G. French, J. L. Elliott, S. E. Levine, *Icarus*, in press.
23. N. F. Ness *et al.*, *Science* **233**, 85 (1986).
24. J. T. Clarke *et al.*, *J. Geophys. Res.*, in press.
25. R. V. Yelle and B. R. Sandel, *Geophys. Res. Lett.* **13**, 89 (1986).

26. We thank R. S. Polidan, J. T. Clarke, and J. H. Waite for helpful discussions and the Voyager Project personnel at the Jet Propulsion Laboratory for the enthusiastic efforts that have made this mission successful. Supported by the Jet Propulsion Laboratory, California Institute of Technology, under NASA contract NAS 7-100. Additional support was provided by the Planetary Sciences Discipline of NASA's Office of Space Sciences under contracts NAGW-610, NSG-7404, and NAGW-649.

28 March 1986; accepted 5 May 1986

Voyager 2 Radio Science Observations of the Uranian System: Atmosphere, Rings, and Satellites

G. L. Tyler, D. N. Sweetnam, J. D. Anderson, J. K. Campbell, V. R. Eshleman, D. P. Hinson, G. S. Levy, G. F. Lindal, E. A. Marouf, R. A. Simpson

Voyager 2 radio occultation measurements of the Uranian atmosphere were obtained between 2 and 7 degrees south latitude. Initial atmospheric temperature profiles extend from pressures of 10 to 900 millibars over a height range of about 100 kilometers. Comparison of radio and infrared results yields mole fractions near the tropopause of 0.85 and 0.15 ± 0.05 for molecular hydrogen and helium, respectively, if no other components are present; for this composition the tropopause is at about 52 kelvins and 110 millibars. Distinctive features in the signal intensity measurements for pressures above 900 millibars strongly favor model atmospheres that include a cloud deck of methane ice. Modeling of the intensity measurements for the cloud region and below indicates that the cloud base is near 1,300 millibars and 81 kelvins and yields an initial methane mole fraction of about 0.02 for the deep atmosphere. Scintillations in signal intensity indicate small-scale structure throughout the stratosphere and upper troposphere. As judged from data obtained during occultation ingress, the ionosphere consists of a multilayer structure that includes two distinct layers at 2,000 and 3,500 kilometers above the 100-millibar level and an extended topside that may reach altitudes of 10,000 kilometers or more. Occultation measurements of the nine previously known rings at wavelengths of 3.6 and 13 centimeters show characteristic values of optical depth between about 0.8 and 8; the maximum value occurs in the outer region of the ϵ ring, near its periapsis. Forward-scattered signals from this ring have properties that differ from those of any of Saturn's rings, and they are inconsistent with a discrete scattering object or local (three-dimensional) assemblies of orbiting objects. These signals suggest a new kind of planetary ring feature characterized by highly ordered cylindrical substructures of radial scale on the order of meters and azimuthal scale of kilometers or more. From radio data alone the mass of the Uranian system is GM_{sys} = 5,794,547 ± 60 cubic kilometers per square second; from a combination of radio and optical navigation data the mass of Uranus alone is GM_U = 5,793,939 ± 60 cubic kilometers per square second. From all available Voyager data, including imaging radii, the mean uncompressed density of the five major satellites is 1.40 ± 0.07 grams per cubic centimeter; this value is consistent with a solar mix of material and apparently rules out a cometary origin of the satellites.

VOYAGER RADIO SCIENCE (RSS) investigations at Uranus included radio occultation studies of the atmosphere and rings and radio tracking studies of the gravity of Uranus and its satellites. Experimental and analytical techniques were the same as those used at Jupiter and Saturn (*1*), with extensions to improve resolution in the case of ring occultation and technical changes in the ground tracking stations to array antennas for increased signal strength.

The Uranus occultations were carried out at wavelengths of 3.6 and 13 cm with the use of unmodulated carriers from the dual-frequency radio subsystem (*2*). During the closest approach of Voyager 2 to Uranus and during the occultations, data were obtained with the 34- and 64-m antennas at the NASA Canberra Deep Space Communications Complex and simultaneously with the 64-m antenna at the Parkes Radio Astronomy Observatory (*3*). These initial results are based on analysis of a subset of the data consisting of those observations available from the automatic systems normally employed for mission tracking, control, and telemetry (*4*) plus the primary recordings (*5*) from the ring occultation period.

Atmosphere of Uranus. During the planetary occultation, radio signals propagating from Voyager 2 to Earth were refracted in the equatorial atmosphere by an angle that was a maximum of 3.1° near midoccultation (*6*) (Fig. 1). Except for a few brief signal drop-outs, the real-time monitors detected signals at both 3.6 cm and 13 cm throughout the occultation interval. These observations are sensitive to the thermal structure and the composition of the atmosphere at pressures between about 1 mbar and 2 to 3 bar. From the initial analysis of the data, we conclude that the range of atmospheric pressures probed in these measurements includes a cloud deck of methane ice crystals and extends well below the base of this cloud layer.

The helium abundance is an important parameter for constraining models of the origin, evolution, and internal structure of the giant outer planets (*7*). Its value in the atmosphere of Uranus is inferred by using high-resolution temperature-pressure (T-p) profiles from inversion of the radio occultation data (*8*) to compute model infrared spectra for various assumed compositions. Comparison of the computed brightness spectra with the Voyager infrared observations at wavenumbers from 200 to 400 cm^{-1} yields an estimate of the atmospheric mean molecular mass near the tropopause (*9*). The most probable composition corresponding to this mass is a mole fraction for H_2 of 0.85 ± 0.05, with He making up the remainder (0.15 ± 0.05) (*10*). It is possible to give only a limited interpretation of this result because of the relatively large uncertainties in the initial measurement and because model atmospheres with other plausible compositions, including traces of nitrogen for example, could produce the observed mean mass with less helium. Nevertheless, the Voyager result represents a significant improvement over previous estimates, such as the helium mole fraction of 0.4 ± 0.2 inferred recently from the terrestrially observed thermal spectrum (*11*). From this new result, we conclude that the helium abundance in Uranus' atmosphere is considerably greater than that in Saturn's outer envelope but roughly comparable with the Jovian and solar values (*12*); however, an enhancement in helium on Uranus by a few tens of percent relative to the solar mixture is still a distinct possibility (*7*).

Figure 2 shows two T-p profiles obtained from analysis of 13-cm data acquired during occultation immersion and emersion. The immersion and emersion profiles have been combined because they cover nearly the same latitudes—88° and 83° from the sun-facing pole, respectively—and agree within the uncertainty of each measurement (2 K) at all pressures. As in earlier studies of Jupiter and Saturn (*13*), the refractivity of the atmosphere is assumed to be constant along geodetic surfaces within the region probed. A rotation period of 17 hours is assumed for the equatorial atmosphere (*14*). In general, the results in Fig. 2 confirm the predictions of earlier radiative-convective equilibrium models (*15*).

The lower parts of the T-p profiles in Fig. 2 represent extreme assumptions concerning the composition of the atmosphere. The solid curve was obtained by adopting the helium and hydrogen fractions above and excluding methane altogether, and the dashed curve shows the result of adding a maximum amount of methane to the gas mixture. For the latter case, the methane abundance corresponds to saturation from the tropopause downward to a pressure of roughly 800 mbar. At that point it is necessary to limit the methane mixing ratio to about 1% by volume to avoid a superadiabatic temperature lapse rate in the lower profile (to 900 mbar) computed from the radio refractivity data (*16*). This is an indication that the troposphere above the 900-mbar level is not fully saturated in methane, but it does not constrain the methane abundance deep in the atmosphere. Assumed compositions in which the methane partial pressure is nonzero but below saturation yield profiles between the two examples in Fig. 2. The maximum pressure in this T-p profile is limited by the performance of the real-time receivers, which were unable to track the signal in thin layers at pressures slightly greater than 900 mbar during both immersion and emersion.

The adiabatic temperature lapse rate depends, through the specific heat, on the gas temperature, the hydrogen ortho-para ratio, and the ortho-para conversion rate. Three scenarios have been suggested for the behavior of hydrogen in the atmospheres of the outer planets (*17*). For "normal" hydrogen the ortho-para ratio is 3:1, and transitions are forbidden. For "intermediate" hydrogen the populations are in equilibrium at the average local temperature, but the conversion rate is too slow for any response to adiabatic changes during convection. For "equilibrium" hydrogen conversion is relatively fast, resulting in equilibrium throughout the adiabatic process. The computed lapse rates for either normal or intermediate hydrogen are consistent with both tempera-

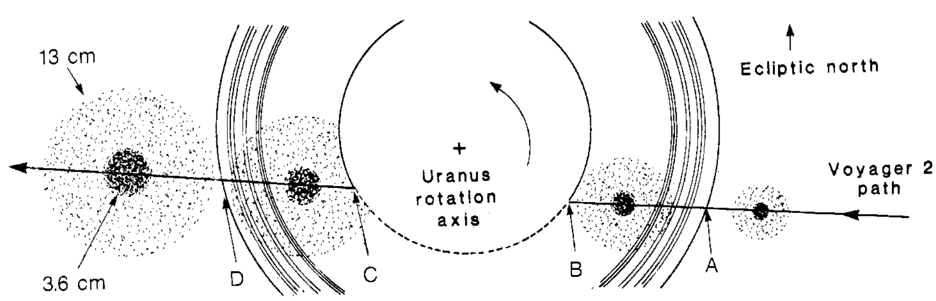

Fig. 1. Earth view of the encounter geometry, which provided occultations by the atmosphere and rings. Shaded circles show the antenna beam projected onto Uranus' equatorial plane at the two wavelengths. Occultation data were recorded continuously over the interval shown. Radio tracking data were obtained over a longer period (approximately 24 hours) which included the closest approach to Miranda at approximately 17:03 universal time (U.T.), spacecraft event time, 24 January. Event times for the points marked A to D are about 19:43, 20:36, 21:59, and 22:53 U.T., respectively. In describing the two sets of occultations by the rings, we refer to the two ring events beginning with A and ending with D as ring immersion and emersion, respectively.

G. L. Tyler, V. R. Eshleman, D. P. Hinson, E. A. Marouf, R. A. Simpson, Center for Radar Astronomy, Stanford University, Stanford, CA 94305.
D. N. Sweetnam, J. D. Anderson, J. K. Campbell, G. S. Levy, G. F. Lindal, Jet Propulsion Laboratory, California Institute of Technology, Pasadena, CA 91109.

ture profiles in Fig. 2. An atmosphere of equilibrium hydrogen, however, is incompatible with the measurements in that the lapse rates would become super-adiabatic for pressures exceeding about 600 mbar. Because the appearance of hydrogen quadrupole lines is difficult to reconcile with normal hydrogen, our result supports an earlier conclusion (*18*) that the behavior of hydrogen on Uranus in the region above the clouds corresponds to the intermediate state.

To obtain initial information about the atmospheric structure and composition at pressures greater than 900 mbar, we constructed model profiles for various assumed fractions of methane deep in the atmosphere. In extrapolating downward from profiles that lie between the two extremes shown in Fig. 2, it is assumed that the lapse rate first transfers to a saturated methane adiabat below the 900-mbar level and then follows this adiabat within a cloud layer. When the local vapor pressure reaches the assumed mixing ratio (the cloud base), the profile shifts abruptly to the dry adiabat. Model predictions for signal intensity vary with both the methane mixing ratio and the thermal structure within the cloud, so that comparisons with the observed intensity over the entire occultation period constrain these parameters.

It is particularly significant that the model predictions exhibit two distinctive features that also appear in the intensity data: (i) a marked decrease in intensity accompanies signal propagation through the saturated region where clouds form, and (ii) an abrupt enhancement in intensity occurs when the lowest point on the propagation path becomes tangent to the cloud base. The former is the result of the refractivity gradient within the cloud where the cycling of latent heat influences the atmosphere's thermal structure; the latter is associated with the change in temperature lapse rate at the cloud base. The model that shows best agreement with the observations has a cloud base at a pressure of about 1300 mbar, where the temperature is about 81 K. Under these conditions the cloud is composed of methane ice crystals, and the methane mole fraction below the clouds is about 0.02. In addition, the decrease in intensity observed near the upper boundary of the cloud region favors models with a rapid transition to a saturated adiabat near 1000 mbar, a pressure that corresponds to the cloud tops. It is likely that direct inversion of the radio data will yield *T-p* profiles to pressures greater than 900 mbar, so that refinements of these values are expected.

Scintillations in signal intensity were observed at both 3.6 cm and 13 cm throughout the occultation, revealing considerable small-scale atmospheric structure such as would be caused by turbulence or internal gravity waves. These scintillation data offer the prospect for remote sensing of atmospheric dynamics and will be studied in the next stage of analysis (*19*).

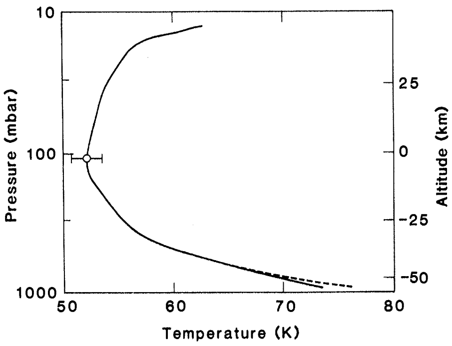

Fig. 2. Temperature plotted against pressure in the equatorial atmosphere of Uranus from inversion of radio occultation data at 13 cm. Profiles from immersion and emersion have been averaged here, since they agree to within the uncertainty of each measurement (2 K) and apply to nearly the same latitudes (see text). Solid and dashed curves reflect different assumptions about atmospheric composition: the former corresponds to H_2 and He fractions of 0.85 and 0.15, respectively, with no other components; the latter shows the effect of adding to the mixture as much methane as possible while still avoiding super-saturation and super-adiabatic lapse rates in retrieved profiles.

Ionosphere of Uranus. Ionospheric data were obtained in the intervals above the neutral atmosphere at both occultation immersion and emersion. Our discussion is limited to initial results at immersion, however, because the real-time data were ambiguous with regard to the ionosphere at emersion.

We observed clear signatures of well-separated, narrow ionospheric layers at altitudes of approximately 2000 and 3500 km above the 100-mbar level in both the real-time data and in initial power spectra from the primary data. Such sharp layers have been detected at Jupiter and Saturn and may be similar to sporadic E layers on Earth (*13, 20*). An extended ionospheric layer may reach altitudes of 10,000 km or more, with a peak density of several thousand electrons per cubic centimeter. However, interpretation of the data pertaining to the topmost layer is somewhat uncertain because of a large variation in the background plasma content that is probably associated with the solar wind. Thus no ionospheric profiles are given at this time.

Rings of Uranus. Ring occultation data were obtained on both sides of the planet (Fig. 1). Our initial results are based on reduction of dual-frequency data from the 64-m antenna at Canberra, which covered the region of the previously known rings. These data have been corrected for diffraction and examined at an effective radial resolution of 200 m (*21*).

The nine previously known rings were readily detected and studied at both 3.6 cm and 13 cm in the radio data—the first time that they have been observed at centimeter wavelengths. The characteristic maximum normal radio depths (τ) observed for each

Table 1. Ring characteristics at 3.6 cm and 13 cm. Symbols in last column: N.D., no clear difference in optical depth with wavelength when a lower SN ratio at 13 cm is considered; (+) or (−), the integrated optical depth at 13 cm is greater (or less) than that at 3.6 cm, typically by about 15% to 20%.

Ring	Position (degrees)*		Width of core feature† (km)	Optical depth			
				Maximum‡		Integrated (τ km)§	
	Emersion	Immersion		3.6 cm	13 cm	3.6 cm	13 cm
6	2		1.7	0.8	0.8	0.9	N.D.
		144	1.9	1.1	1.0	0.9	N.D.
5	7		2.5	2.3	1.5	2.0	—
		149	3.2	1.2	1.2	1.9	N.D.
4		71	2.2	1.5	1.2	1.6	N.D.
	289		2.9	1.3	1.2	1.4	N.D.
α		124	12.4	1.0	1.0	6.1	N.D.
	340		4.7	2.5	2.5	6.5	N.D.
β		14	7.4	1.0	1.0	4.2	N.D.
	230		11.6	0.5	0.5	4.2	—
η		–	1.9	1.0	0.7	1.0	N.D.
	–		1.9	1.0	1.1	0.9	N.D.
γ	–		2.0	6.9	6.3	6.0	N.D.
		–	4.0	4	3.8	9.4	+
δ	–		3.1	4	4	4.1	N.D.
		–	7.0	1.2	1.2	5.3	+
ϵ		30	22.6	8	5	96.	75.
	241		75.0	2.5	2.5	97.	97.

*Approximate positions in orbit measured from periapsis for each ring (*47*); values are not given for the η, γ, and δ rings because they are uncertain. †Excludes extended component. ‡Characteristic normal optical depth at 200-m effective resolution. §Integral of normal optical depth over apparent core of "radio" ring (*23*).

ring vary from approximately 0.8 to 8 (Table 1). The upper range of these values is surprisingly large (*22*), indicating that the Uranian ring system contains substantial amounts of material in the form of particles having sizes comparable to or larger than the radio wavelengths. In addition, there are a number of other, weak observations of possible rings.

We focus further discussion on the ϵ ring because it displays a number of properties found in the others as well as a newly discovered scattering phenomenon. Figure 3 displays results for points near periapsis and quadrature in the orbit of the ring particles, corrected for diffraction at a resolution of 1.0 km. The change in width of the ring with location is readily apparent. Although the large-scale morphology of the ring at the two observation points is similar, there are significant changes in the internal small-scale structure. Near periapsis (Fig. 3A), τ is typically 2.5 to 3, with a maximum of about 8 at 3.6 cm. Signals at the two wavelengths are differentially attenuated at the point of maximum τ. Near quadrature (Fig. 3B), τ is approximately 1 and increases to about 2.5 near both edges. Integrated values of extinction across the ϵ ring (Table 1) differ by about 1% at 3.6 cm and by about 23% at 13 cm (*23*).

The almost complete independence of the integrated extinction over a 3.3:1 variation in width requires that the extinction efficiency of the individual particles be conserved around the ring. We know of no way in which this can be achieved in regions of τ significantly greater than 1 by other than a collection of well-separated particles (*24*). It follows that the ϵ ring must have a considerable thickness normal to the ring orbital plane (*25*). Furthermore, the differences in detailed radial structure between immersion and emersion indicate structure that varies markedly with the true anomalies of particles in their orbits.

Considerable small-scale structure in the ϵ ring is revealed at 200-m resolution (Fig. 3B, inset). A wavelike feature can be identified over 6 to 9 km from the left edge of the inset. A similar structure has been found at about the same relative position in the immersion data.

An unexpected aspect of the ϵ ring observations has been detection of strong near-forward scattering at 3.6 cm as Voyager passed behind the ring near quadrature on occultation emersion. Such scattering has not been detected from the ϵ ring near periapsis, nor has it been observed during either occultation at 13 cm. It has not been seen in connection with any other ring at either wavelength at Uranus or Saturn.

The ϵ ring data have been plotted as a time sequence of power spectra. The scattered signal appears in the spectra as a single localized feature of bandwidth approximately 100 Hz drifting at about -5 Hz sec^{-1} with respect to the directly propagating signal. The total received scattered power is about 0.5% that of the direct signal. It persists for a time that coincides with passage of the spacecraft antenna beam over the ϵ ring. Although the scattering is clearly associated with the ϵ ring, we can rule out scattering by independent discrete objects and three-dimensional collections of objects. Scattered signals from objects in Keplerian orbits within or near the ϵ ring would drift in frequency at three times the observed rate; the actual Doppler signature requires that the scattering center move radially outward or in a retrograde orbit (or both). Further, the large power received requires that the radar cross section of the scattering center be approximately 6×10^{15} m^2—an impossibly large value for a localized scattering center (*26*).

We may be able to explain this anomalous signal in terms of organized structure within ϵ ring rather than by scattering from a discrete object. By presuming that the scatter originates from elongated structure, possibly canted to the azimuthal coordinate, we obtain a match to the frequency drift and a correspondence with the observed bandwidth. The signal strength and duration suggest that the effective scale along the ring of this structure be comparable to or larger than the Fresnel scale (~2 km) and that the

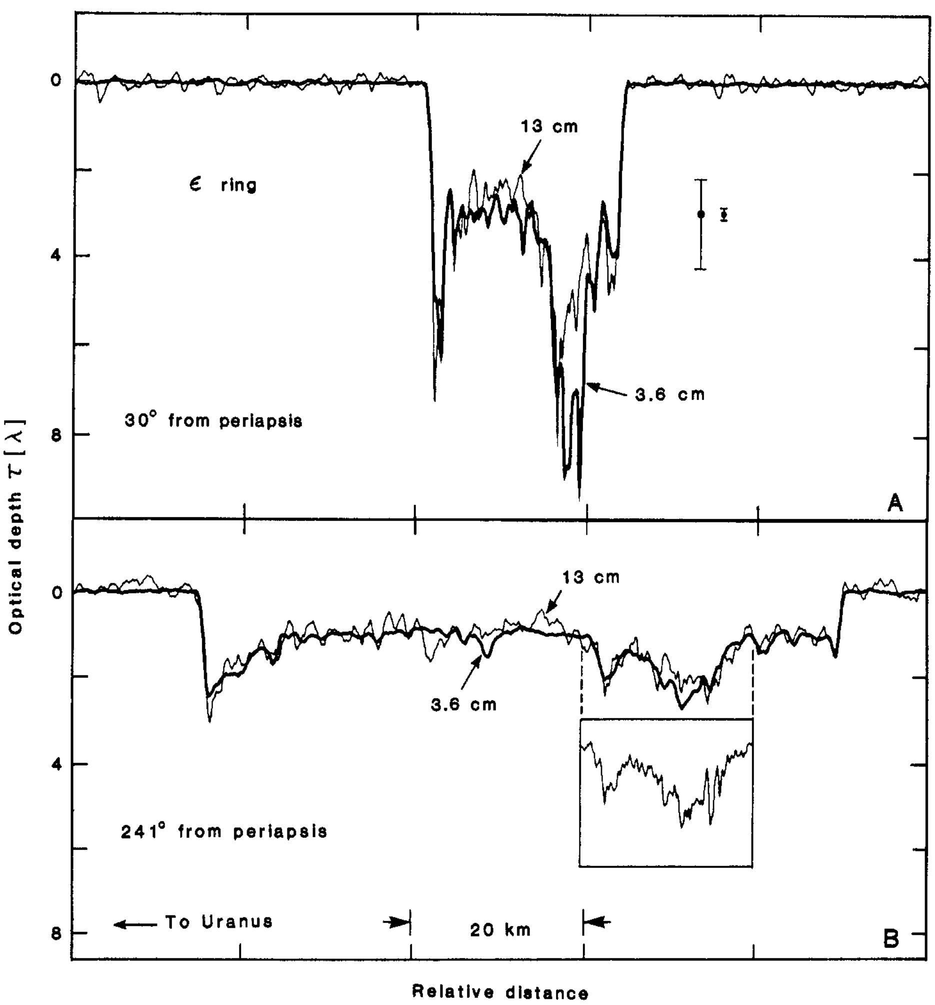

Fig. 3. Profiles of the ϵ ring observed at 3.6 cm (thick line) and 13 cm (thin line). (A) A cut approximately 30° from ring periapsis at a time when Voyager 2 was about 150,000 km behind the rings on the immersion side of Uranus. Significant structure is seen across the ring, the most prominent being the region close to the outer edge where optical depth attains the unusually large value of about 8. Signals at the two wavelengths are differentially affected over much of the ring. (B) Similar profiles corresponding to a cut approximately 241° from periapsis when Voyager was about 290,000 km behind the ring on the emersion side of Uranus. Uncertainties shown in (A) apply at $\tau = 3$ and are less (greater) for smaller (larger) values of τ; similar uncertainties apply in (B), not shown. The larger uncertainty is for $\lambda = 13$ cm. The main profiles are reconstructed from diffracted data to have an effective radial resolution of about 1 km at both wavelengths. This resolution is chosen as a compromise between detail and SN; (inset) 200-m resolution at 3.6 cm. Only relative radial scale is shown because the geometric solution has not been finalized.

radial scale be on the order of meters; the scattering source is thus essentially two-dimensional. We find the indications for such ordered structure within ϵ ring to be extremely intriguing as well as somewhat paradoxical in view of the apparent lack of order in the larger scale extinction profiles shown in Fig. 3. Physical mechanisms invoked to explain the azimuthal asymmetry observed in Saturn's A ring may be relevant (*27*).

Table 1 also gives values for the other previously known rings. Most of the observations show no clear differences in integrated depth at the two wavelengths; further comparison awaits more complete analysis of the relatively noisy 13-cm profiles. Two measurements show larger integrated τ at 3.6 cm; two others, however, show higher integrated τ at 13 cm, which is puzzling. No ring shows strong wavelength variation at both radio measurement locations.

Mass of Uranus. The Voyager 2 determination of the mass of Uranus is connected with the determination of several parameters of the gravity field of the Uranian system. The mass of the system (planet plus satellites) is determined directly from the radio data. The mass of the planet alone, however, must be derived from the total system mass by using relatively imprecise measurements of the satellite masses. The mass of the planet alone is limited by uncertainties in the masses of the individual satellites, particularly Ariel, which is largely inseparable from that of the planet.

We estimate the mass of the total system to be $GM_{sys} = 5{,}794{,}547 \pm 60$ km^3 sec^{-2}, which corresponds to a mass ratio of the sun to the Uranus system (M_{sys}^{-1}) of 22,902.99 ± 0.24. The uncertainty represents a realistic 1σ uncertainty from the radio data and is a significant improvement over previous determinations (*28*). The mass of the planet alone as estimated from the radio data is $GM_U = 5{,}793{,}961 \pm 60$ km^3 sec^{-2}, where the uncertainty is dominated by the uncertainty in the mass of Ariel. If information about satellite masses from the optical navigation is added to the radio measurements, then the value obtained for the mass of the planet is GM_U = 5,793,939 ± 60 km^3 sec^{-2} (*28*).

After Uranus' discovery by Herschel in 1781, the mass of the Uranian system was determined by its effect on the orbit of Saturn and by measurements of the orbital radii and periods of its four largest satellites. The early satellite determinations (*29*) were made before the discovery of Ariel and Umbriel in 1851. The first determinations to include estimates of uncertainty were made from satellite data by Newcomb (*30*) and from the motion of Saturn by Hill (*31*).

Table 2. Satellite masses and densities from a combination of Voyager 2 radio and optical data.

Satellite	GM (km^3 sec^{-2})*	Radius (km)†	Density (g cm^{-3})‡	
			Compressed	Uncompressed§
Miranda	5. ± 1.5	242. ± 5	1.26 ± 0.4	1.26
Ariel	90. ± 16	580. ± 5	1.65 ± 0.3	1.55
Umbriel	85. ± 16	595. ± 10	1.44 ± 0.3	1.35
Titania	232. ± 12	805. ± 5	1.59 ± 0.1	1.42
Oberon	195. ± 11	775. ± 10	1.50 ± 0.1	1.34

*Adopted values of *GM* from this work. †From (*39*). ‡Mass divided by the volume of a sphere of equivalent radius. §Effects of self-compression are removed (*42*).

More recent determinations from satellites (*32*) and from the motion of Saturn (*33*) do not agree within their stated uncertainties (*34*). The value of M_{sys}^{-1} of 22,869, adopted in 1898 by Newcomb (*35*) for the *American Ephemeris and Nautical Almanac* is within 0.15% of the value obtained from the Voyager 2 flyby of Uranus.

Satellite masses. There are no valid estimates of the Uranian satellite masses from before the Voyager encounter (*36*). Miranda's small size dictated that its mass be determined from the direct gravitational effect on Voyager 2 during Voyager's closest approach to the satellite. The determination of the masses of the other large satellites depended on getting as long an arc of tracking data as possible near Uranus so that the indirect effect of the satellites on Voyager—which results from their effect on the barycentric motion of the Uranian system—could be derived from the perturbations in spacecraft velocity along the line of sight (*37*).

The radio data provide the primary information about the mass of Miranda and about a linear combination of the other four satellites, particularly the sum of the masses of Umbriel, Titania, and Oberon (*38*). From the radio data alone we obtain a value for the sum of the masses of these outer three satellites of $GM_{2,3,4} = 477 \pm 25$ km^3 sec^{-2}. Using the summed volumes from the imaging results (*39*) of the three outer satellites, we obtain a mean density for the three satellites of 1.42 ± 0.08 g cm^{-3}. Although this result is obtained from the radio data without the direct benefit of the optical navigation data, there is an indirect dependence in that optically determined, numerically integrated satellite ephemerides are used without adjustment in obtaining these solutions (*40*).

When the optical navigation data are added to the radio-only solution for the gravity parameters, improvements in the satellite masses are realized. This improvement results from determination of mutual perturbations in the satellite system obtained from numerical integration of that system (*41*). We summarize the estimated masses from the combined radio and optical data in Table 2. Also shown are the densities corresponding to the radii as determined by ISS (*39*) plus the uncompressed densities, where the uncertainties are the same as those for the compressed densities (*42*).

The Uranian system may share a common solar composition with the other outer planets, differentiated only by temperature effects on condensation during formation (*43*). Although it may have been too warm for methane to condense at the distance of Uranus from the sun, almost certainly the satellites formed below the condensation temperature of clathrated methane. This may account for the observed methane in the Uranian system (*44*). The density of the outer three satellites is consistent with a value of 1.49 g cm^{-3}, which is obtained for the three satellites on the assumption of a solar mix of 32% rock, 53% water ice, 7% ammonia ice, and 8% methane clathrate hydrate [$(CH_4)\cdot(6H_2O)$] (*42*). The measured mean density of the outer three satellites is inconsistent with an uncompressed density of about 1.8 g cm^{-3}, which is appropriate to condensation from a water-poor or presolar atmosphere in which carbon is present as CO and nitrogen appears as N_2 (*45*). The sum of the *GM*'s for the five satellites is 607 ± 28 km^3 sec^{-2}, and the volume corresponding to the uncompressed material is (6.5 ± 0.1) × 10^{24} cm^3, with a resulting mean uncompressed density of the satellite system of 1.40 ± 0.07 g cm^{-3}. On the basis of these determinations, it is unlikely that the uncompressed density of the mix of constituents in the satellite system is greater than 1.5 or less than 1.3. This density is consistent with the solar mix mentioned above with methane completely locked up in methane clathrate hydrate.

Gravity field of Uranus. The Voyager 2 flyby, at a closest distance of 107,160 km from Uranus, was not favorable for a determination of the nonspherical components of the gravity field. We obtained a relatively weak determination of the lowest degree hydrostatic component from a combination of radio and optical navigation data of $J_2 = (3345 \pm 18) \times 10^{-6}$. Here, J_4 was fixed at the value determined by ring precession, the pole was fixed by the satellite plane, and all other gravity harmonics were set to zero. Our value for J_2 confirms earlier results from ring studies, which have smaller uncertainties (*46*). In addition, the agreement increases our confidence that the other gravity parameters are correctly determined from the flyby.

REFERENCES AND NOTES

1. V. R. Eshleman *et al.*, *Space Sci. Rev.* **21**, 207 (1977); V. R. Eshleman *et al.*, *Science* **204**, 976 (1979); V. R. Eshleman *et al.*, *ibid.* **206**, 959 (1979); G. L. Tyler *et al.*, *ibid.* **212**, 201 (1981); G. L. Tyler *et al.*, *ibid.* **215**, 553 (1982).
2. R. E. Edelson *et al.*, *Science* **204**, 913 (1979).
3. Signal-to-noise (SN) ratios on the order of 50,000 and 3,000 were achieved at 3.6 and 13 cm, respectively, from the Canberra DSN 64-m antenna with 1-second coherent integration intervals. Subsequent combination of data from Canberra and Parkes should improve the SN ratio at 3.6 cm by 3 dB; combination of data from the two Canberra antennas should improve the SN ratio at 13 cm by about 1 dB. Equipment at Parkes was shared [from CSIRO (Commonwealth Scientific and Industrial Research Organisation), ESA (European Space Agency), and NASA].
4. These include real-time measurements of the signal amplitude, frequency, and frequency dispersion at coarse time resolution.
5. Primary data for radio propagation consist of sample measurements of signals at the antenna terminals recorded on computer-compatible tape at rates between 50,000 and 80,000 samples per second.
6. From Earth-view, the virtual radio image of the spacecraft followed the dashed track along the planet's limb indicated in Fig. 1. In the central portion of the occultation, the angle of refraction exceeded the width of the spacecraft antenna beam at both wavelengths; hence the experiment required a continuous maneuver to point the spacecraft antenna at the planet's limb.
7. J. B. Pollack, M. Podolak, P. Bodenheimer, B. Christofferson, in preparation.
8. G. Fjeldbo *et al.*, *Astron. J.* **76**, 123 (1971).
9. Computations of the infrared brightness spectra were performed by B. Conrath and D. Gautier [R. Hanel *et al.*, *Science* **233**, 70 (1986)] using data from coordinated IRIS and RSS observations in the equatorial regions of the atmosphere.
10. The He fraction, 0.15 ± 0.05, corresponds to 52 ± 2.5 K for the temperature minimum at the tropopause.
11. G. S. Orton, *Science* **231**, 836 (1986).
12. B. J. Conrath *et al.*, *Astrophys. J.* **282**, 807 (1984).
13. G. F. Lindal *et al.*, *J. Geophys. Res.* **86**, 8721 (1981); G. F. Lindal *et al.*, *Astron. J.* **90**, 1136 (1985).
14. As of this writing, no moving cloud features have been reported at this latitude.
15. See, for example, J. F. Appleby, *Icarus*, in press, particularly model "c" of Fig. 2 therein.
16. The approach used here is the same as that employed in the analysis of the Titan data; for a more detailed discussion see G. F. Lindal *et al.*, *Icarus* **53**, 348 (1983).
17. S. T. Massie and D. M. Hunten, *ibid.* **49**, 213 (1982); B. J. Conrath and P. J. Gierasch, *ibid.* **57**, 184 (1984).
18. L. Trafton, *Astrophys. J.* **207**, 1007 (1976); L. Wallace, *Icarus* **43**, 231 (1980); J. T. Bergstralh and K. H. Baines, in *Uranus and Neptune*, J. T. Bergstralh, Ed. (*NASA Conf. Publ. 2330*, 1984), p. 179; G. S. Orton and J. F. Appleby, *ibid.*, p. 89.
19. See, for example, D. P. Hinson, *J. Geophys. Res.* **89**, 65 (1984); ——— and G. L. Tyler, *Icarus* **54**, 337 (1983).
20. R. H. Chen, *J. Geophys. Res.* **86**, 7792 (1981).
21. For theory of radio ring occultation and analysis see E. A. Marouf *et al.*, *Icarus* **49**, 161 (1982); E. A. Marouf *et al.*, in preparation; H. A. Zebker, thesis, Stanford University (1984).
22. Earth-based studies of Uranus' rings by stellar occultations provide only lower bounds on the optical depth of the six unresolved rings 6, 5, 4, η, γ, and δ [see, for example, J. L. Elliot and P. D. Nicholson, in *Planetary Rings*, R. Greenberg and A. Brahic, Eds. (Univ. of Arizona Press, Tucson, 1985), pp. 25–72]. The maximum optical depth observed at radio wavelengths (Table 1) often exceeds these bounds. Secondary broad components associated with the η and δ rings [J. L. Elliot *et al.*, *Astron. J.* **86**, 444 (1981)] were also observed in the radio data. The prominent structure of the 3.6-cm profile of the ϵ ring, shown in Fig. 3B at 1-km resolution, corresponds to features observed from Earth [see Fig. 4 of P. D. Nicholson *et al.*, *Astron. J.* **87**, 433 (1982)].
23. The quantity calculated is $\Sigma\tau(r_i,\lambda)\Delta r$, where r is distance from Uranus across each ring, λ is wavelength, and τ is corrected for the obliquity. The resolution Δr chosen for each particular case varied between 200 and 1000 m, depending on the width of the ring and the SN ratio. It was reported at a Voyager press briefing, 27 January 1986, that the ϵ ring displayed no wavelength dependence; this statement applies to the data in Fig. 3B; those in Fig. 3A had not been examined.
24. Because the ring material is spread over a large area, by more than 3:1 between (A) and (B) of Fig. 3, independently scattering (that is, well-spaced) particles will show a decrease in the total optical depth by the same factor. This is observed in a general way between (A) and (B) but not in detail. At 3.6 cm the unchanged value of the integrated extinction indicates that the extinction per particle has been conserved, assuming that the particles themselves are unchanged; a similar, albeit weaker, result is observed at 13 cm.
25. For independent scattering, the minimum particle separation in the direction of propagation should be about ten diameters or more for each unit of τ. For $\tau = 2$ to 8 observed here, the extension of the ring would be several tens of diameters. Strict radiative transfer–type models typically have volume fractions less than 10^{-3}, which would imply an even thicker extended ring.
26. The radar cross section of a rough dielectric sphere, such as a planet or satellite, is of the order (radius)^2. To account for the present observation, such an object would need to be larger than Uranus itself.
27. Both Earth-based and spacecraft observations show that Saturn's A ring exhibits an azimuthally asymmetric reflectivity [see, for example, H. J. Reitsema *et al.*, *Astron. J.* **81**, 209 (1976); B. A. Smith *et al.*, *Science* **215**, 504 (1981)]. G. Colombo *et al.* [*Nature (London)* **264**, 344 (1976)] suggest that the asymmetry is due to trailing density wakes of embedded large particles. See also W. H. Julian and A. Toomre, *Astrophys. J.* **146**, 810 (1966); F. A. Franklin and G. Colombo, *Icarus* **33**, 279 (1978).
28. A combination of radio and optical navigation data yields an additional factor of 2 improvement in the mass determination for the Uranian system, but we are reluctant to recommend the smaller uncertainty until the relative weighting of the two data types is better understood. System mass obtained from the radio data alone does not correlate with any other parameters and is reliable. Determining the mass of the planet alone depends on knowing the sum of the masses of the five principal satellites, which requires optical navigation data for highest accuracy. For our more accurate planet mass we used a fit to optical and radio data, but we increased the uncertainty significantly with respect to the formal uncertainty to allow for a possible incorrect relative weighting of the two data types.
29. O. Struve, *Mon. Not. R. Astron. Soc.* **8**, 44 (1848); J. C. Adams, *ibid.* **9**, 159 (1849).
30. S. Newcomb [*U.S. Nav. Obs. App.* **1**, 7 (1875)] obtained a value for M_{sys}^{-1} of 22,600 ± 150.
31. G. W. Hill [*Astron. J.* **19**, 157 (1898); *Astron. Pap. Am. Ephem.* 7 (1898)] obtained a value for M_{sys}^{-1} of 23,239 ± 132.
32. D. L. Harris, thesis, University of Chicago (1950); D. W. Dunham, thesis, Yale University (1971).
33. W. J. Klepczynski *et al.*, *Astron. J.* **75**, 739 (1970).
34. The determination of M_{sys}^{-1} of 22,900 ± 200 from meridian circle and radar range observations of the planets [M. E. Ash, I. I. Shapiro, W. B. Smith, *Science* **174**, 551 (1971)] probably represents the best that can be accomplished with planetary perturbations.
35. S. Newcomb, *Astron. Pap. Am. Ephem.* **6** (1898); *ibid.* 7 (1898). Newcomb's value was also used recently in a study of ephemerides [X. X. Newhall *et al.*, *Astron. Astrophys.* **125**, 150 (1983)].
36. S. F. Dermott and P. D. Nicholson, *Bull. Am. Astron. Soc.* **17**, 742 (1986); *Nature (London)*, in press.
37. We have neglected the mass of the material in the rings and the Uranian satellites newly discovered by Voyager. We estimate the total mass of this material to be less than 1 km^3 sec^{-2}.
38. The strong constraint placed on the mass of the total system, GM_{sys}, and on the five satellite masses by the radio data is $0.2966(GM_{sys} - 5{,}794{,}523.4) + 0.1241(GM_1 - 81.3) - 0.5090(GM_2 - 74.2) - 0.1110(GM_3 - 249.6) - 0.5012(GM_4 - 153.2) - 0.0220(GM_5 - 4.0) = 0.0 \pm 7.3$ km^3 sec^{-2}, where the subscripts refer to Ariel, Umbriel, Titania, Oberon, and Miranda, respectively, and G is the universal gravitational constant. This constraint is satisfied by solutions given here.
39. B. A. Smith *et al.*, *Science* **233**, 43 (1986).
40. The sum of the masses of the three outer satellites as determined from radio data alone is recommended over a similar sum obtained from a combination of radio and optical data. The reason is the same as that given in (*28*).
41. We used the most recent numerically integrated satellite ephemerides for this work (from R. A. Jacobson, personal communication).
42. Uncompressed densities are based on the solar mix given in the text, a uniform satellite temperature of 60 K at the current epoch (corresponding to an albedo of 0.25), and homogeneous density. The rocky component is assumed to have an uncompressed density of 3.361 g cm^{-3} [M. J. Lupo, *Icarus* **52**, 40 (1982)]. The value for compressed water ice is from M. J. Lupo and J. S. Lewis [*ibid.* **40**, 157 (1979)]. Determinations of density eliminate compositional classes that fall outside the range of the uncertainties in the densities. In this sense, the suggestion of CH_4-dominance over CO in the protoplanetary phase [J. S. Lewis and R. G. Prinn, *Astrophys. J.* **238**, 357 (1980); R. G. Prinn and B. Fegley, *ibid.* **249**, 308 (1981)] represents a viable model. J. B. Pollack [in *Protostars and Planets*, D. C. Black and M. S. Matthews, Eds. (Univ. of Arizona Press, Tucson, 1985), pp. 791–831] considers compositional classes consistent with solar composition but differentiated by temperature and pressure conditions of formation.
43. J. S. Lewis, *Earth Planet. Sci. Lett.* **15**, 286 (1974).
44. A. J. R. Prentice, *Phys. Lett. A* **114**, 211 (1986).
45. D. J. Stevenson [*NASA Conf. Publ. 2330*, 1984, p. 409] considers a number of generic satellite compositions, including a possible Uranian class of rock plus $(CO,N_2)\cdot(7H_2O)$=ice clathrate with an uncompressed density of about 1.8 g cm^{-3}. A cometary composition has been suggested by R. Greenberg *et al.* [*Icarus* **59**, 87 (1984)]. If we assume that the satellites of Uranus form a single compositional class, our results rule out both of these high-density models. Self-compression in the two outer satellites would result in densities well in excess of 2.0 g cm^{-3}, contrary to our measurements.
46. J. L. Elliot, in *Uranus and the Outer Planets*, G. Hunt, Ed. (Cambridge Univ. Press, Cambridge, England, 1982), pp. 237–256; P. D. Nicholson *et al.*, *Astron. J.* **87**, 433 (1982).
47. P. D. Nicholson, personal communication.

48. This experiment required extensive support from the Voyager Project and the NASA DSN, both at the Jet Propulsion Laboratory, and at the Deep Space Communication Complexes, especially in Australia, where the normal tracking facilities were augmented for Voyager by the inclusion of the Parkes Radio Astronomy Observatory. We thank these groups for their efforts in obtaining the data discussed here. Design, implementation, and execution of these experiments required the skills, creativity, and dedicated efforts of a number of individuals. The RSS support team—R. Kursinski, S. Borutzki, M. Connally, P. Eshe, H. Hotz, S. Kinslow, and K. Moyd—was responsible for coordination of activities between the Voyager project and the DSN, implementation of the observational strategy, and monitoring of the execution. F. Donivan managed this activity within the DSN. D. L. Gresh and P. A. Rosen designed and implemented much of the software necessary for planning and for data reduction. J. Lyons provided computational support in obtaining the atmospheric profiles. Essential computing equipment at Stanford was a gift of Data General Corporation. Supported by funding from NASA.

27 March 1986; accepted 5 May 1986